

RESEARCH ARTICLE

Open Access



Cine MR feature tracking analysis for diagnosing thymic epithelial tumors: a feasibility study

Koji Takumi^{1*} , Hiroaki Nagano¹, Akie Mukai¹, Kazuhiro Ueda², Kazuhiro Tabata³ and Takashi Yoshiura¹

Abstract

Background To assess the feasibility of the cine MR feature tracking technique for the evaluation of cardiovascular-induced morphological deformation in the diagnosis of thymic epithelial tumors (TETs).

Methods Our study population consisted of 43 patients with pathologically proven TETs including 10 low-grade thymomas, 23 high-grade thymomas, and 10 thymic carcinomas. Cine MR images were acquired using a balanced steady-state free precession sequence with short periods of breath-hold in the axial and oblique planes in the slice with the largest lesion cross-sectional area. The tumor margin was manually delineated in the diastolic phase and was automatically tracked for all other cardiac phases. The change rates of the long-to-short diameter ratio (Δ LSR) and tumor area (Δ area) associated with pulsation were compared between the three pathological groups using the Kruskal–Wallis H test and the Mann–Whitney U test. A receiver-operating characteristic (ROC) curve analysis was performed to assess the ability of each parameter to differentiate thymic carcinomas from thymomas.

Results Δ LSR and Δ area were significantly different among the three groups in the axial plane ($p=0.028$ and 0.006 , respectively) and in the oblique plane ($p=0.034$ and 0.043 , respectively). Δ LSR and Δ area values were significantly lower in thymic carcinomas than in thymomas in the axial plane (for both, $p=0.012$) and in the oblique plane ($p=0.015$ and 0.011 , respectively). The area under the ROC curves for Δ LSR and Δ area for the diagnosis of thymic carcinoma ranged from 0.755 to 0.764.

Conclusions Evaluation of morphological deformation using cine-MR feature tracking analysis can help diagnose histopathological subtypes of TETs and identify thymic carcinomas preoperatively.

Keywords Thymic epithelial tumors, Thymic cancer, Cine magnetic resonance imaging, Feature tracking

*Correspondence:

Koji Takumi

takumi@m2.kufm.kagoshima-u.ac.jp

¹Department of Radiology, Kagoshima University Graduate School of Medical and Dental Sciences, 8-35-1 Sakuragaoka, Kagoshima City 890-8544, Japan

²General Thoracic Surgery, Kagoshima University Graduate School of Medical and Dental Sciences, 8-35-1 Sakuragaoka, Kagoshima City 890-8544, Japan

³Human Pathology, Kagoshima University Graduate School of Medical and Dental Sciences, 8-35-1 Sakuragaoka, Kagoshima City 890-8544, Japan



© The Author(s) 2023. **Open Access** This article is licensed under a Creative Commons Attribution 4.0 International License, which permits use, sharing, adaptation, distribution and reproduction in any medium or format, as long as you give appropriate credit to the original author(s) and the source, provide a link to the Creative Commons licence, and indicate if changes were made. The images or other third party material in this article are included in the article's Creative Commons licence, unless indicated otherwise in a credit line to the material. If material is not included in the article's Creative Commons licence and your intended use is not permitted by statutory regulation or exceeds the permitted use, you will need to obtain permission directly from the copyright holder. To view a copy of this licence, visit <http://creativecommons.org/licenses/by/4.0/>. The Creative Commons Public Domain Dedication waiver (<http://creativecommons.org/publicdomain/zero/1.0/>) applies to the data made available in this article, unless otherwise stated in a credit line to the data.

Background

Thymic epithelial tumors (TETs) are the most common primary tumors in the anterior mediastinum, with an incidence of approximately 1.3 per million person-years [1]. Clinically, TETs comprise three subgroups according to the WHO classification: low-risk thymomas (type A, AB, and B1), high-risk thymomas (type B2 and B3), and thymic carcinomas. Subgroup is an independent prognostic factor for survival in patients with TETs [2] and is important information for optimizing treatment strategies.

Cine MR imaging is widely used to evaluate cardiovascular diseases by assessment of cardiac morphology and function [3] and can also be used to diagnose chest wall or cardiovascular invasion of thoracic masses by evaluating cardiovascular-induced sliding motion [4–6]. The MR feature tracking technique, a two-dimensional post-processing algorithm based on cine MRI, has recently been introduced into clinical practice. It was developed to evaluate cardiac function and myocardial deformation, which are applied to the diagnosis and prediction of prognosis in cardiac diseases [7]. A recent report [8] showed that MR feature tracking analysis of cardiovascular-induced liver deformation was correlated with liver damage in patients with tetralogy of Fallot. Reduced passive deformity of the liver may be due to chronic liver damage with fibrosis. Therefore, the feature tracking technique may have the potential to provide information on tissue stiffness by evaluation of morphological deformation of a mediastinal lesion (including TETs) that occurs by the pulsation of adjacent cardiovascular structures. The WHO classification of TETs is determined pathologically based on the morphological manifestations of epithelial cells and the ratio of lymphocytes to epithelial cells [9], which can impact tumor stiffness. We hypothesize that evaluation of cardiovascular-induced morphological deformation using cine-MR feature tracking analysis can assist in diagnosing the histopathological classification of TETs. Therefore, the purpose of this study was to assess the diagnostic feasibility of feature tracking analyses using pretreatment cine-MR images for the evaluation of TETs.

Materials and methods

Patients

Institutional ethics review board approval was obtained and informed consent was waived for this retrospective study. Between February 2008 and April 2021, all patients who met the following inclusion criteria were enrolled: (a) pathologically confirmed TET, (b) had undergone cine-MR examination, (c) no history of treatment for TET before the MR examination, and (d) lesions larger than 10 mm in short diameter. The final diagnosis was determined by histological examination of biopsy or

surgical specimens. The tissues were fixed with 10% neutral phosphate-buffered formalin, routinely processed for paraffin embedding, and sectioned for hematoxylin and eosin (HE) staining. All TET lesions were classified into six histological subtypes according to the 2015 WHO histological classification and divided into the following three subgroups: low-risk thymoma (types A, AB, and B1), high-risk thymoma (types B2 and B3), and thymic carcinoma.

MR imaging protocol

All MR examinations were performed using 3T systems (Trio, Siemens Healthcare, Erlangen, Germany; or Ingenia 3.0T, Philips Healthcare, Best, The Netherlands) using a 30-channel phased-array body coil during a breath hold. Cine-MR imaging has been a part of our institute's routine clinical pretreatment MR protocol for the evaluation of chest wall or cardiovascular invasion in anterior mediastinal tumors. Cardiac-gated cine images were acquired using a balanced steady-state free precession (bSSFP) sequence with short periods of breath holding in the axial and oblique planes. The oblique plane was applied perpendicular to the interface between the thymic lesion and the adjacent cardiovascular structures with reference to the axial image. The following parameters were used for imaging in both planes: repetition time, 10 to 48 ms; echo time, 1.5 ms; flip angle, 45 or 50°; turbo field echo factor, 22; number of cardiac phases, 20–25; number of signal averages, 1; field of view, 350×350 mm; in-plane spatial resolution, 1 to 2×1 to 2 mm; section thickness, 3–6 mm; number of slices, 3–5.

Imaging analyses

To evaluate cardiac-induced deformation with feature tracking evaluations, all cine images were transferred and analyzed using a workstation (Ziostation 2; Ziosoft Inc., Tokyo, Japan). All images were independently evaluated by a radiologist (with 20 years of chest radiology experience) who was blinded to the final pathological results. All measurements were performed twice by the same observer. The tumor margin was delineated manually in the diastolic phase in the axial and oblique planes on the slice with the largest cross-sectional area of the lesion, and automatically tracked for all other cardiac phases using feature-tracking methods based mainly on a block-matching approach, which defines the region of interest for the target structure and tracks it along the cardiac cycle by searching for the most similar region in the next image [10, 11]. Tumor sizes (longest and shortest diameters) and lesion area were automatically measured for all cardiac phases. We calculated the long-to-short-diameter ratio, which was defined as the short diameter divided by the long diameter. Long diameter (LD_{max} and LD_{min}), short diameter (SD_{max} and SD_{min}), long-to-short

diameter ratio (LSR_{max} and LSR_{min}), and lesion area (LA_{max} and LA_{min}) were recorded in the two phases when the lesion areas were maximal and minimal, respectively. We also calculated the change in the long-to-short-diameter ratio (Δ long-to-short-diameter ratio [ΔLSR]) and lesion area (Δ area) between the two phases when the lesion areas were maximal and minimal. The length of contact between the lesion and the adjacent cardiovascular structures was measured in both planes.

Statistical analysis

Intra-observer agreement was assessed by calculating the intra-class correlation coefficient (ICC). ICCs were considered to indicate excellent agreement when >0.74 [12]. Long diameter (LD_{max} and LD_{min}), short diameter (SD_{max} and SD_{min}), long-to-short diameter ratio (LSR_{max} and LSR_{min}), lesion area (LA_{max} and LA_{min}), ΔLSR , and Δ area were compared among the three groups (low- and high-risk thymomas and thymic carcinomas), between low- and high-risk thymomas, and between all thymomas and thymic carcinomas using the Kruskal–Wallis H test or the Mann–Whitney U test. Receiver-operating characteristic (ROC) curve analysis was performed to evaluate the ability of continuous values to differentiate thymic carcinomas from thymomas. Sensitivity and specificity were calculated using a threshold criterion that would maximize the Youden index. All data for continuous variables are presented as mean \pm standard deviation. Values

of $P < 0.05$ were considered indicative of significance in all analyses. Statistical analyses were performed using MedCalc version 19.6 (MedCalc Software, Mariakerke, Belgium) and SPSS version 28.0 (SPSS, Chicago, IL).

Results

Patients and thymic tumor classifications

Forty-three eligible patients (18 men, 25 women; mean age, 62.3 ± 15.4 years; range, 25–85 years) were identified and included in this study (Fig. 1). The clinical and pathological characteristics of the study population are summarized in Table 1. The subgroups of TETs were diagnosed pathologically as 10 low-risk thymomas (type A [n=4], AB [n=3], type B1 [n=3]), 23 high-risk thymomas (type B2 [n=8], type B3 [n=15]), and 10 thymic carcinomas. All thymic tumors were located in the anterior mediastinum.

Feature tracking parameters among the three TET groups

Intra-observer variability was excellent for all parameters (Online supplementary table). Table 2 lists the values of tracking parameters in the axial and oblique images according to group. There was no significant difference among the groups in terms of contact length between the lesion and adjacent cardiovascular structures in either plane (both $p > 0.05$). ΔLSR and Δ area were significantly different among the three groups in the axial plane ($p = 0.028$ and 0.006 , respectively) and in the oblique

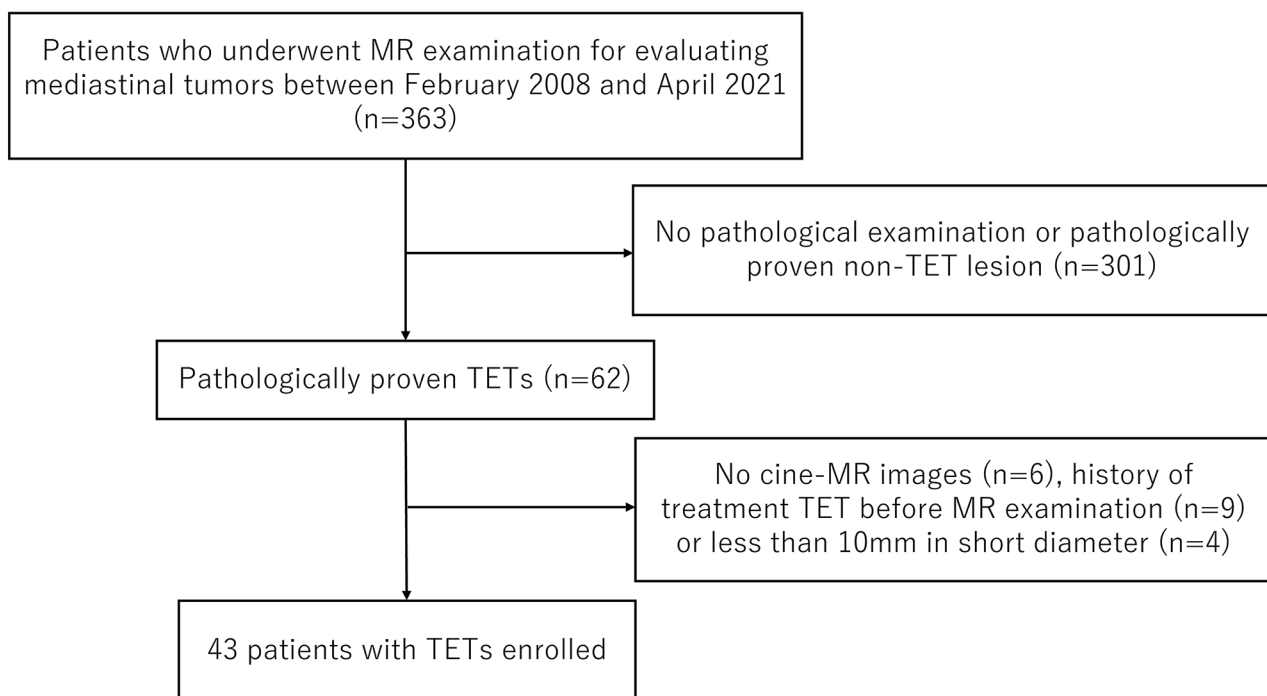


Fig. 1 Flow diagram of the study population. Abbreviation: TET = thymic epithelial tumor

Table 1 Clinical and demographic characteristics

Variables	N=43
Gender (M: F)	18:25
Age (mean ± SD)	62.3 ± 15.4
Major clinical symptoms	
Pain or pressure in the chest	6
Shortness of breath	1
General fatigue	3
Facial swelling	2
Weight loss	1
Drooping eyelids	9
No symptom	21
Mosaoka-Koga stage	
I	9
II	19
III	9
IV	6
WHO classification	
A	4
AB	3
B1	3
B2	8
B3	15
Carcinoma	10

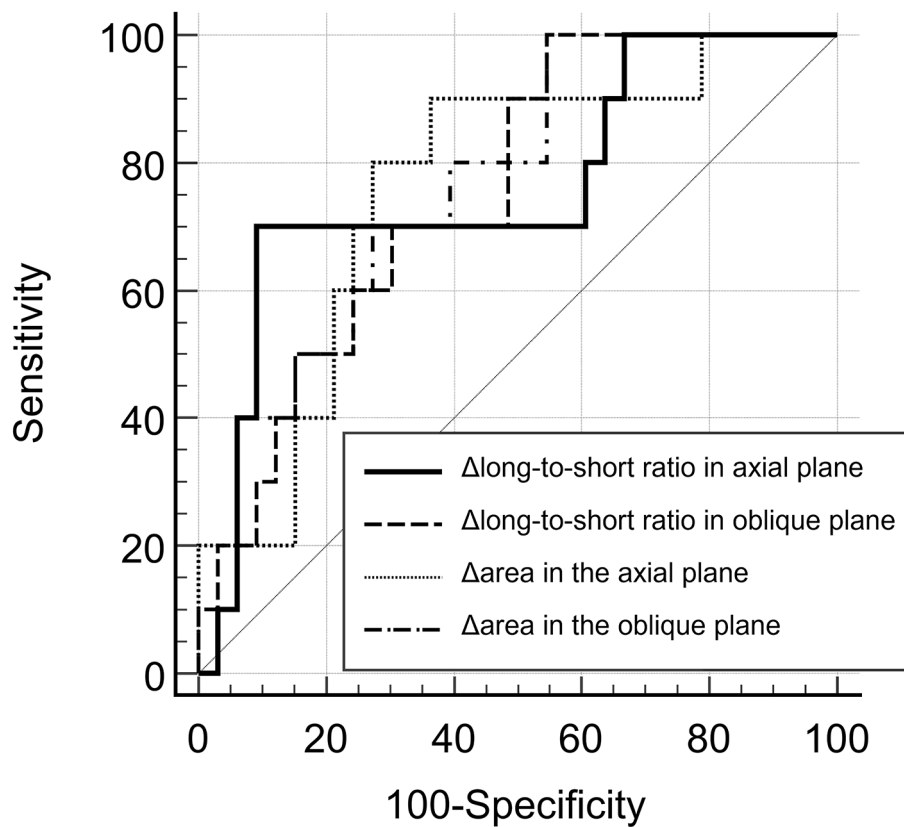


Fig. 2 ROC curve analysis of different parameters for diagnosing thymic carcinoma. The area under the ROC curve values were 0.761, 0.755, 0.761, and 0.764 for Δ LSR in the axial and oblique planes, and Δ area in the axial and oblique planes, respectively

Table 2 Clinical characteristics and cine MR feature tracking parameters

	Low-risk thymomas (n = 10)	High-risk thymomas (n = 23)	Thymic carcinomas (n = 10)	P (among three groups)	P (Low- vs. high-risk thymomas)	P (all thymomas vs. carcinomas)
Axial image						
Contact length (mm)	43.2 ± 14.6	33.9 ± 13.5	44.0 ± 16.3	0.101	0.089	0.204
Long diameter with maximum lesion area (mm)	49.5 ± 16.4	45.2 ± 16.8	52.9 ± 22.9	0.721	0.524	0.702
Short diameter with maximum lesion area (mm)	30.5 ± 12.0	23.3 ± 9.1	33.5 ± 18.7	0.123	0.105	0.249
Long-to-short ratio with maximum lesion area	0.6 ± 0.1	0.5 ± 0.1	0.6 ± 0.1	0.193	0.133	0.386
Long diameter with minimum lesion area (mm)	48.6 ± 16.7	44.7 ± 16.7	52.5 ± 23.0	0.724	0.550	0.661
Short diameter with minimum lesion area (mm)	28.7 ± 11.5	22.5 ± 9.4	32.9 ± 18.9	0.140	0.155	0.194
Long-to-short ratio with minimum lesion area	0.6 ± 0.1	0.5 ± 0.2	0.6 ± 0.1	0.241	0.207	0.273
ΔLong-to-short ratio (%)	4.7 ± 3.5	4.1 ± 5.8	1.4 ± 1.4	0.028	0.253	0.012
Maximum lesion area (mm ²)	1349.8 ± 918.3	964.7 ± 654.0	1747.0 ± 1942.0	0.294	0.269	0.313
Minimum lesion area (mm ²)	1270.0 ± 885.9	929.8 ± 649.0	1717.5 ± 1939.1	0.310	0.305	0.286
ΔArea (%)	6.8 ± 4.2	4.9 ± 4.5	2.6 ± 1.6	0.006	0.038	0.012
Oblique image						
Contact length (mm)	54.1 ± 24.1	43.6 ± 16.2	51.2 ± 23.2	0.524	0.269	0.702
Long diameter with maximum lesion area (mm)	51.3 ± 19.5	42.6 ± 14.5	53.8 ± 25.7	0.477	0.305	0.487
Short diameter with maximum lesion area (mm)	30.4 ± 12.5	23.8 ± 10.9	31.7 ± 19.4	0.2829	0.133	0.681
Long-to-short ratio with maximum lesion area	0.6 ± 0.1	0.6 ± 0.2	0.6 ± 0.1	0.800	0.524	0.788
Long diameter with minimum lesion area (mm)	50.1 ± 19.5	42.6 ± 14.5	53.3 ± 25.8	0.533	0.343	0.487
Short diameter with minimum lesion area (mm)	30.4 ± 12.5	23.8 ± 10.9	31.0 ± 18.7	0.266	0.133	0.542
Long-to-short ratio with minimum lesion area	0.6 ± 0.2	0.6 ± 0.2	0.6 ± 0.1	0.772	0.524	0.810
ΔLong-to-short ratio (%)	6.5 ± 5.9	4.6 ± 4.2	1.6 ± 1.0	0.034	0.363	0.015
Maximum lesion area (mm ²)	1339.5 ± 1003.0	950.2 ± 642.4	1704.9 ± 1962.3	0.421	0.305	0.435
Minimum lesion area (mm ²)	1336.9 ± 984.0	900.5 ± 637.4	1670.7 ± 1947.7	0.354	0.384	0.356
ΔArea (%)	5.7 ± 3.7	6.5 ± 4.8	2.8 ± 1.4	0.043	0.862	0.011

Table 3 Area under the ROC curve values for the diagnosis of thymic carcinoma

Parameters	AUC	Threshold Value	Sensitivity (%)	Specificity (%)
ΔLong-to-short ratio in the axial plane	0.761	≤0.90	70.0	90.9
ΔLong-to-short ratio in the oblique plane	0.755	≤3.53	100.0	45.5
ΔArea in the axial plane	0.761	≤3.39	90.0	63.6
ΔArea in the oblique plane	0.764	≤5.04	100.0	45.5

plane ($p=0.034$ and 0.043 , respectively), whereas there was no significant difference in long diameter (LD_{max} and LD_{min}), short diameter (SD_{max} and SD_{min}), long-to-short diameter ratio (LSR_{max} and LSR_{min}), or lesion area (LA_{max} and LA_{min}) between the groups in either plane (all $p>0.05$).

Comparison between thymomas and thymic carcinomas

The ΔLSR and $\Delta area$ of thymic carcinomas were significantly smaller than those of thymomas in the axial plane ($4.26\pm 5.13\%$ vs. $1.45\pm 1.42\%$, $p=0.012$; $5.47\pm 4.43\%$ vs. $2.58\pm 1.55\%$, $p=0.012$, respectively) and in the oblique plane ($5.19\pm 4.78\%$ vs. $1.65\pm 0.99\%$, $p=0.015$; $6.21\pm 4.43\%$ vs. $2.82\pm 1.41\%$, $p=0.011$, respectively). For diagnosing

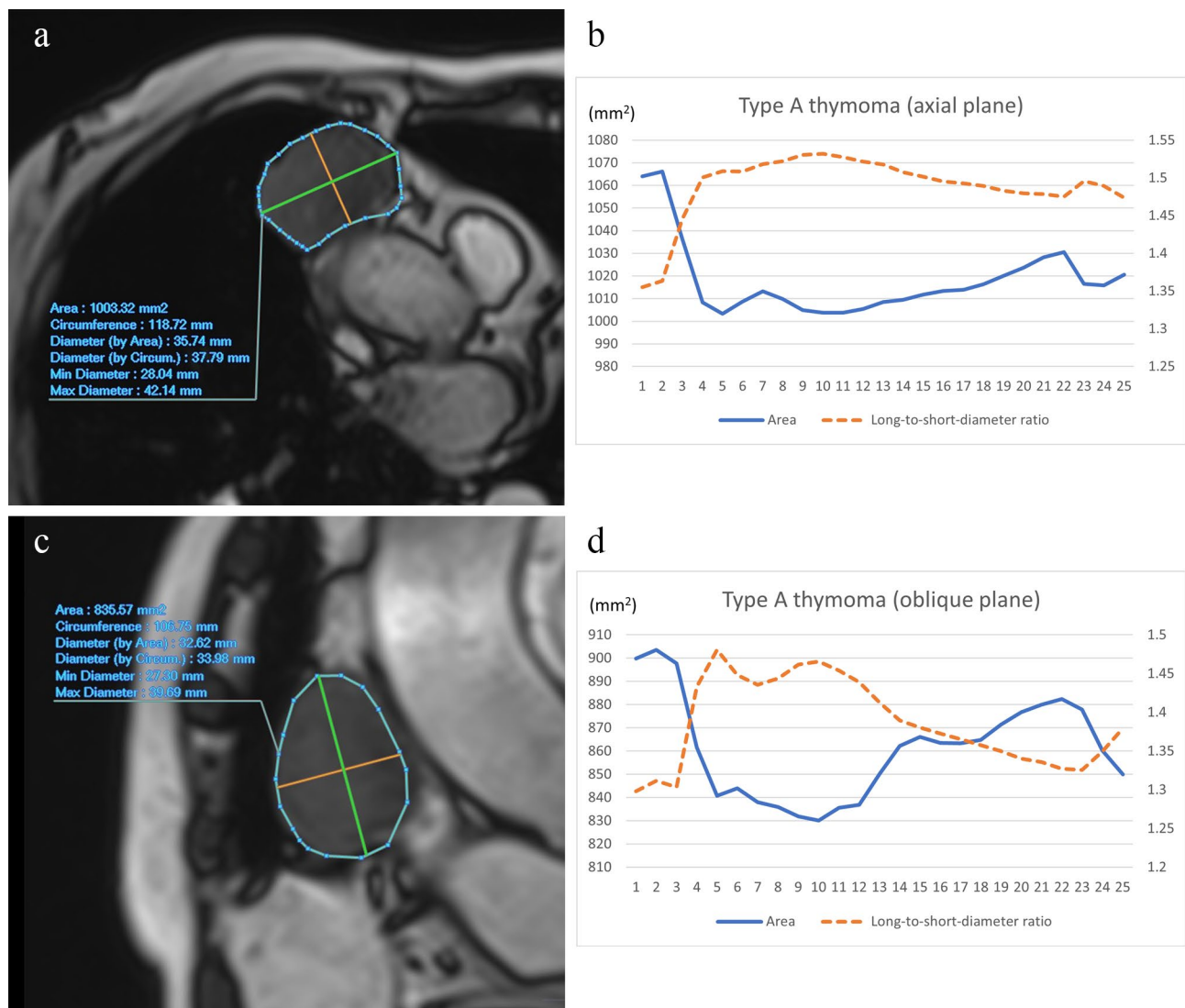


Fig. 3 A 64-year-old woman with low-risk thymoma (type A). Axial (a) and oblique (c) cine MR images of low-risk thymoma (type A) in the right anterior mediastinum, accompanied by graphs representing the time course of area and long-to-short diameter ratio in axial (b) and oblique planes (d). In the axial plane, Δlong-to-short diameter ratio and Δarea were 10.58% and 5.89%, respectively. In the oblique plane, Δlong-to-short diameter ratio and Δarea were 10.50% and 8.14%, respectively

thymic carcinomas, the values of the area under the ROC curve (AUC) were 0.761 (95% confidential interval [CI], 0.606–0.877), 0.755 (95%CI, 0.600–0.873), 0.761 (95%CI, 0.606–0.877), and 0.764 (95%CI, 0.610–0.880) for Δ LSR in the axial and oblique planes, and Δ area in the axial and oblique planes, respectively (Fig. 2; Table 3). The optimal cutoff values of Δ LSR and Δ area in the axial plane to differentiate thymic carcinoma from thymomas were 0.90% (sensitivity, 70.0% with 95%CI of 34.8–93.3; specificity, 90.9% with 95%CI of 75.7–98.1) and 3.39% (sensitivity, 90% with 95%CI of 55.5–99.7; specificity, 63.6% with 95%CI of 45.1–79.6), respectively (Table 3). The optimal cutoff values of Δ LSR and Δ area in the oblique plane to differentiate thymic carcinoma from thymomas were 3.53% (sensitivity, 100.0% with 95%CI of 69.2–100.0; specificity, 45.5% with 95%CI of 28.1–63.6) and 5.04%

(sensitivity, 100% with 95%CI of 69.2–100.0; specificity, 45.5% with 95%CI of 28.1–63.6), respectively (Table 3).

Representative cases are shown in Figs. 3 and 4, and [online-supplementary videos](#).

Association between feature tracking parameters and cystic/necrotic changes or adjacent cardiovascular structures

Cystic/necrotic changes were present in 10 lesions (3 low-risk thymomas, 4 high-risk thymomas, and 3 thymic carcinomas), and in all cases, these changes occupied less than half of the lesion. There was no significant difference between the lesions with and without cystic/necrotic changes in Δ LSR and Δ area in both planes (all, $p > 0.05$).

Twenty-five lesions (3 low-risk thymomas, 17 high-risk thymomas, and 5 thymic carcinomas) predominantly

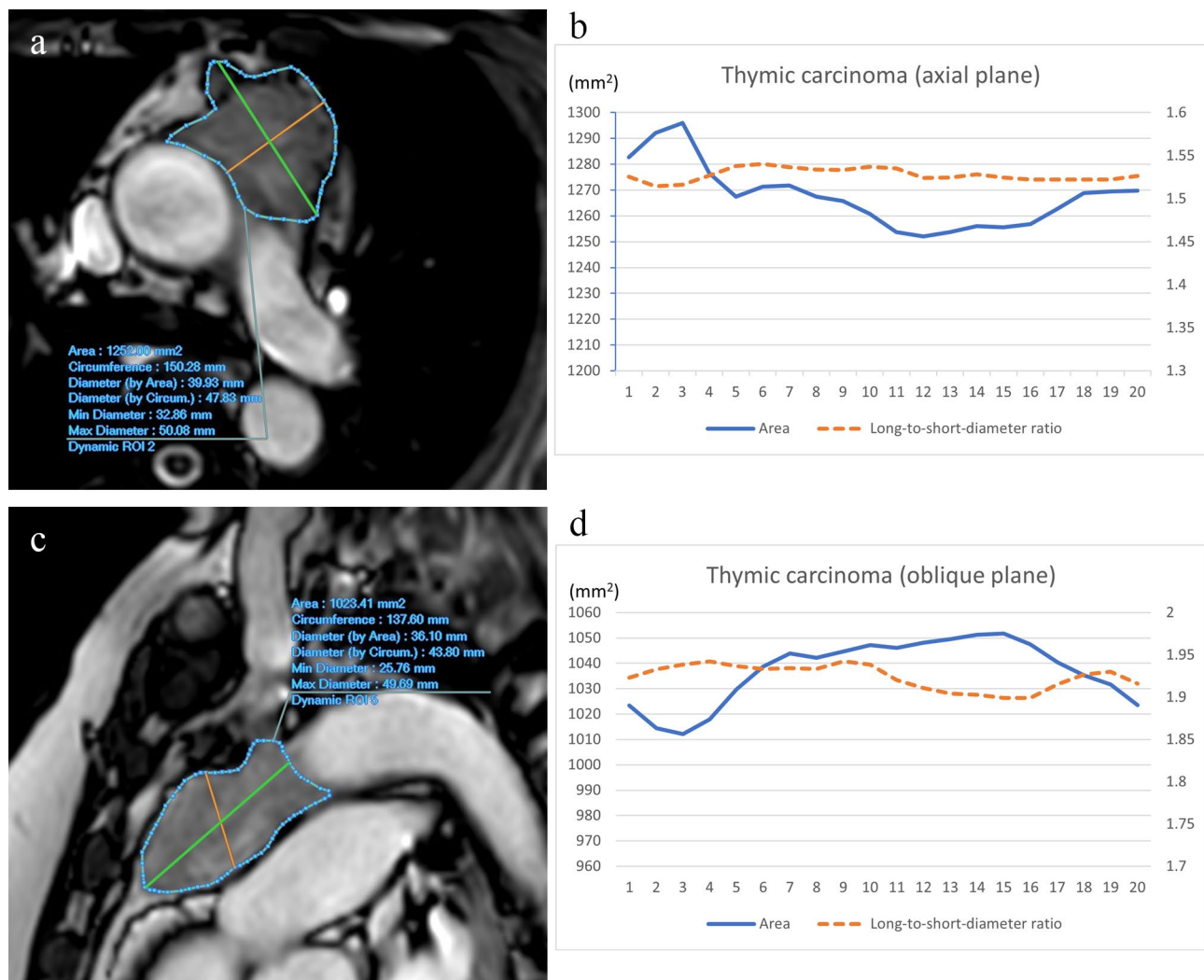


Fig. 4 A 57-year-old woman with thymic carcinoma. Axial (**a**) and oblique (**c**) cine MR images show an irregularly shaped and ill-defined tumor in the anterior mediastinum. Graphs represent the time course of area and long-to-short diameter ratio in axial (**b**) and oblique planes (**d**). In the axial plane, Δ long-to-short diameter ratio and Δ area were 0.52% and 3.39%, respectively. In the oblique plane, Δ long-to-short diameter ratio and Δ area were 2.05% and 3.74%, respectively

contacted the aorta, 12 (4 low-risk thymomas, 5 high-risk thymomas, and 3 thymic carcinomas) predominantly contacted the pulmonary artery, and 6 (3 low-risk thymomas, 1 high-risk thymomas, and 2 thymic carcinomas) predominantly contacted the right atrium. No significant difference was observed among the predominantly contacted adjacent cardiovascular structures in Δ LSR and Δ area in both planes (all, $p > 0.05$).

Discussion

The results of the present study demonstrate the feasibility of cine MRI-based feature tracking analysis for assessing cardiac-induced deformation to diagnose TETs. Values of Δ LSR and Δ area were significantly different between the TET subtypes, and those of thymic carcinomas were significantly smaller than those of thymomas. AUCs for Δ LSR and Δ area to diagnose thymic carcinomas ranged from 0.755 to 0.764. To the best of our knowledge, this potential role of cine-MR feature tracking analysis for diagnosing TETs has not been demonstrated previously.

Tissue stiffness can provide additional information in evaluating several organs [13–17], and radiological approaches such as ultrasound and MR elastographies have been developed for such evaluation [15, 16]. Measurement of liver stiffness using MR elastography is useful to predict the stage of liver fibrosis and long-term progression and outcome in chronic liver disease [15, 17]. Stiffness of the thymus in healthy children evaluated by MR elastography presented a mild negative correlation with age, height, and weight, which can be influenced by changes in the thymic epithelial space and the perivascular space [18]. Cine-MR feature tracking analysis can also provide information on tissue stiffness [8, 19–21], in which tissue deformation is inversely proportional to tissue stiffness. Cardiovascular MR feature tracking to quantify myocardial strain has been reported to be associated with ventricular stiffness [19], and cardiac-induced deformation using cine-MR tagging analysis has been used to assess liver stiffness [20, 21]. Ohashi et al. reported that cardiac-induced liver deformation evaluated by the cine-MR feature tracking technique was associated with liver function in patients with adult congenital heart disease [8]. In the present results, imaging parameters associated with cardiac-induced deformation of TETs, such as Δ LSR and Δ area obtained from cine-MR feature tracking analysis, were significantly different between the histopathological TET groups. The pathological subtypes of TETs according to the WHO classification are characterized by the content of neoplastic epithelial cells and non-neoplastic immature T cells. Typical thymomas, especially type AB, B1, and B2 thymomas, contain an abundance of immature T cells and fewer interstitial cells within the lesion [9],

which can result in lower tumor stiffness compared with lymphocyte-sparse TETs such as B3 thymoma and thymic carcinomas. Therefore, the cine-MR feature tracking technique may enable the assessment of stromal conditions within a lesion and could be particularly useful for evaluating lesions in which the stromal features vary by histological subtype, such as TETs.

Evaluation of lesion stiffness was reported to be useful for differentiation between benign and malignant lesions [22–24]. Malignant tumors tend to have an abundant extracellular matrix, and increased vascularity and interstitial pressure [25]. These characteristics, along with increased cellularity, may cause increased stiffness. In addition, intratumoral fibrosis is highly associated with cancer [26], which can result in increased lesion stiffness compared with benign lesions. In organs such as breast, pancreas, prostate, and lymph nodes, malignant lesions were reported to be stiffer than benign lesions or adjacent parenchymal organ tissue on ultrasound elastography [22–24, 27]. In the thoracic space, US elastography demonstrated that malignant pleural-based masses were also stiffer than benign masses [28]. A preliminary study focused on MR elastography demonstrated that the stiffness level of thymic carcinoma had a tendency to be higher than that of thymoma and lymphoma [29]. In the present results, Δ LSR and Δ area values of thymic carcinomas were significantly lower than those of thymomas, which suggests that the stiffness of thymic carcinoma is higher than that of thymomas, possibly due to the abundant fibrous tissues in these lesions. Cine MRI is a commonly used MR sequence that can be performed on almost any MR device without additional expensive functions. Therefore, it is clinically useful to be able to predict histopathological characteristics by evaluating cardiovascular-induced deformation of TETs at the same time as evaluating cardiovascular invasion [4–6].

There are limitations in the present study. First, we included only a small number of patients with TET from a single institute, which limited the statistical power and universality of the study. In addition, it was a retrospective study that may have been subject to selection bias due to the unbalanced number of patients for each TET subtype. We believe that our pilot study will encourage future research and that a well-designed prospective study with a large number of cases is needed to confirm our findings. Second, cardiac-induced deformation of TETs can be affected by the stiffness of the adjacent cardiovascular structures and by blood pressure. Further research is needed to clarify the relationship between the state of adjacent structures and cardiac-induced deformation.

Conclusion

The present results suggest that cardiac-induced deformation of TETs evaluated using the cine-MR-based feature tracking technique may reflect differences in histopathological characteristics among TETs. Evaluation of morphological deformation using cine MRI can help diagnose histopathological subtypes of TET and identify thymic carcinomas preoperatively.

Abbreviations

TET	Thymic epithelial tumor
WHO	World Health Organization
MRI	Magnetic resonance imaging
bSSFP	Balanced steady-state free precession
LD	Long diameter
SD	Short diameter
LSR	Long-to-short diameter ratio
LA	Lesion area
Δ LSR	Change in long-to-short diameter ratio between the two phases when lesion areas were maximal and minimal
Δ area	Change in lesion area between the two phases when lesion areas were maximal and minimal
ROC	Receiver-operating characteristic
AUC	Area under the ROC curve
ICC	Intraclass correlation coefficient
CI	Confidential interval

Supplementary Information

The online version contains supplementary material available at <https://doi.org/10.1186/s40644-023-00560-z>.

Supplementary Material 1
Supplementary Material 2
Supplementary Material 3
Supplementary Material 4
Supplementary Material 5

Acknowledgements

We thank Mr. Yamato Shimomiya of Ziosoft Inc. for technical assistance.

Authors' contributions

Conception: KT; study design: KT and TY; data collection: HM, AM, KU, and KT; data analysis: KT, and AM; data interpretation: KT and HN, manuscript writing: KT and TY; manuscript editing: All authors. The authors read and approved the final manuscript.

Funding

Not applicable.

Availability of data and materials

The datasets of current study are available from the corresponding author on reasonable request.

Declarations

Ethics approval and consent to participate

This retrospective study was approved by our institutional ethics review board (Ethics Committee on Epidemiological Studies Kagoshima University Graduate School of Medical and Dental Sciences, No. 210040), and the requirement for informed consent of patients was waived.

Consent for publication

Not applicable.

Competing interests

Authors have no conflict of interest.

Received: 8 January 2023 / Accepted: 19 April 2023

Published online: 01 May 2023

References

- Engels EA. Epidemiology of thymoma and associated malignancies. *J Thorac Oncol.* 2010;5:260–5.
- Okuma Y, Hosomi Y, Watanabe K, Yamada Y, Horio H, Maeda Y, et al. Clinicopathological analysis of thymic malignancies with a consistent retrospective database in a single institution: from Tokyo Metropolitan Cancer Center. *BMC Cancer.* 2014;14:349.
- Kramer CM, Barkhausen J, Bucciarelli-Ducci C, Flamm SD, Kim RJ, Nagel E. Standardized cardiovascular magnetic resonance imaging (CMR) protocols: 2020 update. *J Cardiovasc Magn Reson.* 2020;22:17.
- Kajiwara N, Akata S, Uchida O, Usuda J, Ohira T, Kawate N, et al. Cine MRI enables better therapeutic planning than CT in cases of possible lung cancer chest wall invasion. *Lung Cancer.* 2010;69:203–8.
- Seo JS, Kim YJ, Choi BW, Choe KO. Usefulness of magnetic resonance imaging for evaluation of cardiovascular invasion: evaluation of sliding motion between thoracic mass and adjacent structures on cine MR images. *J Magn Reson Imaging.* 2005;22:234–41.
- Panda S, Irodi A, Daniel R, Chacko BR, Vimala LR, Gnanamuthu BR. Utility of cine MRI in evaluation of cardiovascular invasion by mediastinal masses. *Indian J Radiol Imaging.* 2020;30:280–5.
- Amzulescu MS, De Craene M, Langet H, Pasquet A, Vancaeynest D, Pouleur AC, et al. Myocardial strain imaging: review of general principles, validation, and sources of discrepancies. *Eur Heart J Cardiovasc Imaging.* 2019;20:605–19.
- Ohashi R, Nagao M, Ishizaki U, Shiina Y, Inai K, Sakai S. Liver strain using feature Tracking of Cine Cardiac magnetic resonance imaging: Assessment of Liver Dysfunction in patients with Fontan circulation and tetralogy of Fallot. *Pediatr Cardiol.* 2020;41:389–97.
- Marx A, Chan JK, Coindre JM, Detterbeck F, Girard N, Harris NL, et al. The 2015 World Health Organization classification of tumors of the Thymus: continuity and changes. *J Thorac Oncol.* 2015;10:1383–95.
- Claus P, Omar AMS, Pedrizzetti G, Sengupta PP, Nagel E. Tissue Tracking Technology for assessing Cardiac mechanics: principles, normal values, and clinical applications. *JACC Cardiovasc Imaging.* 2015;8:1444–60.
- Pedrizzetti G, Claus P, Kilner PJ, Nagel E. Principles of cardiovascular magnetic resonance feature tracking and echocardiographic speckle tracking for informed clinical use. *J Cardiovasc Magn Reson.* 2016;18:51.
- Shrout PE, Fleiss JL. Intraclass correlations: uses in assessing rater reliability. *Psychol Bull.* 1979;86:420–8.
- Khan S, Fakhouri F, Majeed W, Kolipaka A. Cardiovascular magnetic resonance elastography: a review. *NMR Biomed.* 2018;31:e3853.
- Li M, Guo J, Hu P, Jiang H, Chen J, Hu J, et al. Tomoelastography based on Multifrequency MR Elastography for prostate Cancer detection: comparison with multiparametric MRI. *Radiology.* 2021;299:362–70.
- Guglielmo FF, Venkatesh SK, Mitchell DG. Liver MR Elastography technique and image interpretation: pearls and pitfalls. *Radiographics.* 2019;39:1983–2002.
- Ozturk A, Olson MC, Samir AE, Venkatesh SK. Liver fibrosis assessment: MR and US elastography. *Abdom Radiol (NY).* 2022;47:3037–50.
- Gidener T, Yin M, Dierkhising RA, Allen AM, Ehman RL, Venkatesh SK. Magnetic resonance elastography for prediction of long-term progression and outcome in chronic liver disease: a retrospective study. *Hepatology.* 2022;75:379–90.
- Bayramoğlu Z, Öztürk M, Çalışkan E, Ayyıldız H, Adaletli İ. Normative values of thymus in healthy children; stiffness by shear wave elastography. *Diagn Interv Radiol.* 2020;26:147–52.
- Tello K, Dalmer A, Vanderpool R, Ghofrani HA, Naeije R, Roller F, et al. Cardiac magnetic resonance imaging-based right ventricular strain analysis for Assessment of Coupling and diastolic function in Pulmonary Hypertension. *JACC Cardiovasc Imaging.* 2019;12:2155–64.
- Chouhan MD, Fitzke HE, Bainbridge A, Atkinson D, Halligan S, Davies N, et al. Cardiac-induced liver deformation as a measure of liver stiffness using

- dynamic imaging without magnetization tagging—preclinical proof-of-concept, clinical translation, reproducibility and feasibility in patients with cirrhosis. *Abdom Radiol (NY)*. 2021;46:4660–70.
21. Lefebvre T, Petitclerc L, Hébert M, Bilodeau L, Sebastiani G, Olivé D, et al. MRI cine-tagging of cardiac-induced motion for noninvasive staging of liver fibrosis. *J Magn Reson Imaging*. 2020;51:1570–80.
 22. Huang L, Ma M, Du Z, Liu Z, Gong X. Quantitative evaluation of tissue stiffness around lesion by sound touch elastography in the diagnosis of benign and malignant breast lesions. *PLoS ONE*. 2019;14:e0219943.
 23. Rouvière O, Melodelima C, Hoang Dinh A, Bratan F, Pagnoux G, Sanzalone T, et al. Stiffness of benign and malignant prostate tissue measured by shear-wave elastography: a preliminary study. *Eur Radiol*. 2017;27:1858–66.
 24. Yang JR, Song Y, Jia YL, Ruan LT. Application of multimodal ultrasonography for differentiating benign and malignant cervical lymphadenopathy. *Jpn J Radiol*. 2021;39:938–45.
 25. Jain RK. Barriers to drug delivery in solid tumors. *Sci Am*. 1994;271:58–65.
 26. Yamauchi M, Barker TH, Gibbons DL, Kurie JM. The fibrotic tumor stroma. *J Clin Invest*. 2018;128:16–25.
 27. An H, Shi Y, Guo Q, Liu Y. Test-retest reliability of 3D EPI MR elastography of the pancreas. *Clin Radiol*. 2016;71:1068e1067–1068e1012.
 28. Ozgokce M, Yavuz A, Akbudak I, Durmaz F, Uney I, Aydin Y, et al. Usability of Transthoracic Shear Wave Elastography in differentiation of Subpleural Solid Masses. *Ultrasound Q*. 2018;34:233–7.
 29. Tang W, Huang Y, Wu N, Lu W, Qi L, Wu B. Magnetic resonance elastography of the Anterior Mediastinal Mass at 3T: a preliminary study. *Int Soc Magn Res Med Proc*. 2016;24:2931.

Publisher's Note

Springer Nature remains neutral with regard to jurisdictional claims in published maps and institutional affiliations.